ARCHIVES OF ELECTRICAL ENGINEERING VOL. 60(2), pp. 197-209 (2011)

DOI 10.2478/v10171-011-0019-2

Investigation of the skull melting method for the generation of particulate material of inorganic compounds*

BJÖRN RIEMER, ENNO LANGE, KAY HAMEYER

Institute of Electrical Machines, RWTH Aachen University
Schinkelstrasse 4, D-52062 Aachen, Germany
e-mail: Bjoern.Riemer@IEM.RWTH-Aachen.de

(Received: 02.07.2010, revised: 10.12.2010)

Abstract: This paper describes the application of the skull melting method for an artificial generation of particulate material of inorganic compounds like CsOH, NaOH, SnO_2 and UO_2. The skull melting process is analyzed analytically. Thereby the electromagnetic field is calculated by a one dimensional time harmonic model. Thermal losses are estimated by simple analytical formulas. Finally an electromagnetic thermal field coupling is performed to calculate the temperature distribution inside the crucible, considering transient thermal effects. The skull melting process is simulated for the example of UO_2. Under consideration of the given material properties it is shown that the skull melting method can be applied to fuse UO_2.

Key words: skull melting, cold crucible, electromagnetic thermal field coupling

1. Introduction

For a safety-related evaluation of atomic reactor perturbations, the behavior and spatial distribution of resulting particulate material is of special importance. For an artificial generation of this particulate material the application of the skull melting method to different inorganic target material compounds like CsOH, NaOH, SnO_2 and UO_2 has to be investigated. Above mentioned non radioactive compounds have comparable physical properties to UO_2, so that investigations on the spatial distribution and the sinking velocity of particulate material can be made with this surrogate compounds.

Skull melting is a quasi crucible free inductive heating method where the heating material is charged inside a cylindrical water cooled copper crucible which is surrounded by a water cooled high frequency coil as it is depicted in Figure 1a), [1, 2].

The coil is driven by a current up to a frequency of about 2 MHz. Due to the resulting magnetic field, eddy currents are induced within the target material. As a result of these eddy

* This is extended version of a paper which was presented at the 21st *Symposium on Electromagnetic Phenomena in Nonlinear Circuits*, Essen-Dortmund, 29.06-02.07, 2010.

currents, the heating process is activated due to ohmic losses. An increasing electrical conductivity of the target material with increasing temperature is essential for a successful skull melting process. During the heating process a sinter crust is generated at the cool crucible wall and on top of the melt. This is schematically depicted in Figure 1b). The sinter crust insulates the crucible to the high temperature of the melt and shields the melt from a contamination by possible impurities of the crucible. Due to the lower temperature of the sinter crust and therefore a low electrical conductivity almost no eddy currents are induced into the sinter crust.

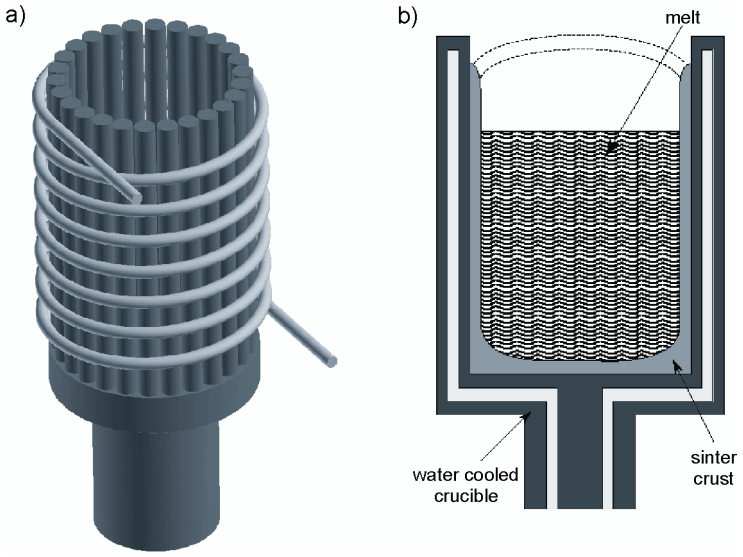

Fig. 1. Model and schematic view of the cold crucible: a) model of the cold crucible with coil; b) schematic view of the crucible

The advantages of the skull melting method are the purity of the melt and the possibility to heat materials up to temperatures above 3000 K.

To investigate the applicability of the skull melting method to the materials mentioned above, the process is analyzed analytically. Based on the specification of the material parameters, the electromagnetic induced power inside the heating material is calculated. Thermal losses due to radiation and heat flow through the sinter crust are analyzed. Finally, a method for the coupling of the electromagnetic and thermal field calculation is presented. Due to the temperature dependent material properties the temperature distribution is calculated by a transient thermal Finite Element model.

2. Material properties

The calculation of the skull melting process requires the knowledge of material properties over the full temperature range up to the boiling point. These data are rarely available. The

best investigated compound of the above mentioned target materials is UO_2. Due to the lack of especially thermal properties, the following investigations are based on UO_2. The melting point of UO_2 is between 2600 K [3] and 3120 K [4] and the boiling point at 3815.1 K. The density ρ differs between 10960 kg/m^3 at 298 K and 10030 kg/m^3 at 2500 K [4]. Because of this small variation, the density is supposed to be constant.

The electromagnetic field calculation of the skull melting process requires the knowledge of the electrical conductivity $\sigma(T)$, the relative permeability $\mu_r(T)$ and the relative permittivity over the whole temperature range up to the boiling point. There have been several investigations of the electrical conductivity of UO_2 e.g. by Bates et al. in 1967 [5], Killeen et al. in 1980 [6] and Casado et al. in 1994 [7]. Confirmed by measurements, Bates and Killeen approximate the electrical conductivity by Arrhenius plots:

$$\sigma(T) = A \cdot e^{-\frac{E_A}{k_B T}}. \tag{1}$$

with the pre-exponential factor A, the Boltzmann constant k_B, the activation energy E_A and the temperature T. Both declared different pre-exponential factors and activation energies for temperatures greater than 1400 K. Casado detected an additional dependency of the electrical conductivity of $T^{-3/2}$ due to the appearance of small-polaron hopping:

$$\sigma(T) = \frac{\sigma_1}{T^{3/2}} \cdot e^{-\frac{E_A}{k_B T}}. \tag{2}$$

His determined conductivity is slightly lower than the data of Bates and Killeen, up to a temperature of 2500 K.

As it can be seen in Figure 2 there is a strong increase of the activation energy nearly 1400 K. This effect occurs due to a transition of extrinsic (p)-conduction for low temperatures to intrinsic (n)-conduction. This effect is documented by all the authors. Because of the uncertainties in the available data this paper deals with the electrical conductivity of Casado for a worstcase estimation for UO_2.

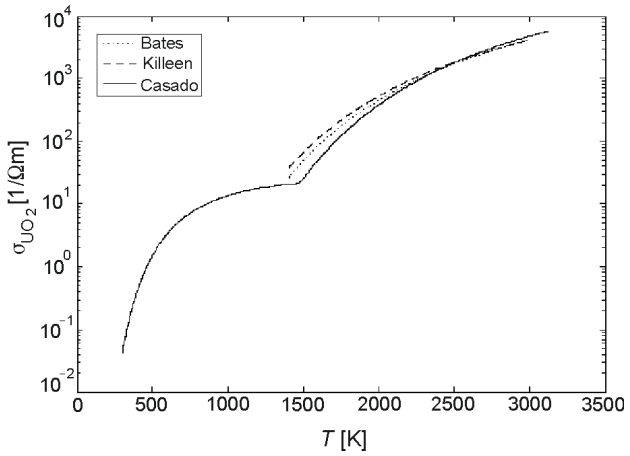

Fig. 2. Electrical conductivity of UO_2

As the materials under consideration do not contain any ferromagnetic components, the relative permeability is assumed to be $\mu_r = 1$. The molar susceptibility of UO_2, which is directly coupled to the relative permeability, has been investigated by Blumenröder et al. [8] for a temperature range 30 K $\leq T \leq$ 400 K. For the available data of this temperature range the assumption is valid.

The relative permittivity was investigated by Hampton et al. in 1985 [9] at room temperature. Hampton identified a frequency dependency of the relative permittivity by:

$$\varepsilon_r(f) = C \cdot f^m, \tag{3}$$

with $C = (9.8 \pm 2.0) \cdot 10^7$ and $m = -0.98 \pm 0.02$. Based on the given data it could be expected that there will be no wave propagation inside the heating material, despite the high frequency by the following estimation. Wave propagation will only occur if the wavelength is shorter then the dimensions of the crucible and thus:

$$\varepsilon_r \geq \left(\frac{c}{f \cdot \lambda}\right)^2 \cdot \frac{1}{\mu_r}, \tag{4}$$

with the light velocity c, the field frequency f and the wavelength $\lambda = 2 \cdot r_{cr}$. For an assumed frequency of about 2 MHz and a crucible radius $r_{cr} = 50$ mm no wave propagation is expected for a value of $\epsilon_r < 2.2 \cdot 10^6$. By this assumption the displacement current density will be neglected for the electromagnetic field calculation.

To calculate the temperature distribution inside the crucible the knowledge of the thermal conductivity and the specific heat capacity is necessary.

Fink had summarized this thermophysical properties in 2000 [4]. The molar heat capacity is given for a temperature range 298.15 K ≤ T ≤ 3210 K by:

$$\begin{aligned} C_{p,mol}(T) = {} & +52.1743 + 87.951\left(\frac{T}{1000}\right) - 84.2411\left(\frac{T}{1000}\right)^2 + \\ & + 31.542\left(\frac{T}{1000}\right)^3 - 2.6334\left(\frac{T}{1000}\right)^4 - 0.7139\left(\frac{T}{1000}\right)^{-2}, \end{aligned} \tag{5}$$

and for 3120 ≤ T ≤ 4500 K by:

$$C_{p,mol}(T) = +0.25136 + \frac{1.3288 \cdot 10^9}{T^2}. \tag{6}$$

The molar heat capacity is in direct relation to the specific heat capacity by:

$$C_p(T) = \frac{C_{p,mol}}{m_{mol}}, \tag{7}$$

with the molar mass of UO_2 $m_{mol} = 270$ g/mol [10]. The specific heat capacity is given in J/kgK. As it is depicted in Figure 3a) the specific heat capacity has a discontinuity at the λ-transition point, where the phase changes from solid to liquid, at 3120 K.

The thermal conductivity is given for a temperature range 298.15 K ≤ T ≤ 3210 K:

$$\lambda(T) = \frac{100}{7.5408 + 17.692 \cdot \left(\frac{T}{1000}\right) + 3.6142 \cdot \left(\frac{T}{1000}\right)^2} + \frac{6400}{\left(\frac{T}{1000}\right)^{\frac{5}{2}}} e^{\frac{-16.35}{\frac{T}{1000}}}. \tag{8}$$

Figure 3b) depicts the thermal conductivity in W/mK.

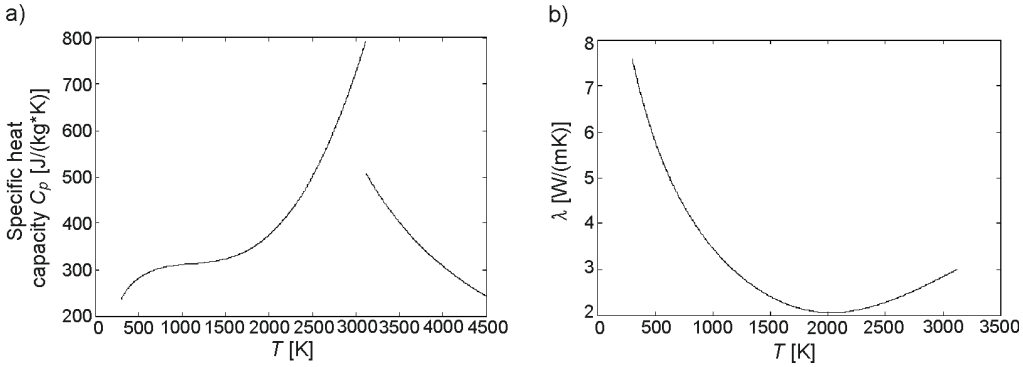

Fig. 3. Thermal properties of UO_2: a) specific heat capacity; b) thermal conductivity

3. Electromagnetic field calculation

A model of a cold crucible with its high frequency coil is depicted in Figure 1a). If the height of the coil is long with respect to the filling height of the target material and all involved materials (crucible, target material) have a non ferromagnetic character, the electromagnetic field inside the target material can be assumed as paraxial. As it is estimated by equation (4) the displacement current density will be neglected. The high frequency coil will be supplied by a resonance generator with a sinusoidal current. So, Maxwell's equations for the harmonic electromagnetic field problem reduce to:

$$\Delta \vec{H} - j\omega\mu\sigma\vec{H} = 0, \tag{9}$$

with the Laplace operator Δ, the magnetic field strength $\vec{H}$, the angular frequency ω and the permeability $\mu = \mu_0 \cdot \mu_r$. Under consideration of

$$\frac{\partial \vec{H}}{\partial \varphi} = 0 \quad \text{and} \quad \frac{\partial \vec{H}}{\partial z} = 0,$$

the induced eddy current density as a function of the radial position r and the time t by:

$$\vec{J}(r,t) = \frac{p \cdot n \cdot \hat{I}}{\mathcal{J}_0(p \cdot r_{me})} \cdot \mathcal{J}_1(p \cdot r) \cdot e^{j\omega t}\vec{e}_\varphi \tag{10}$$

with the magnitude of the coil current $\hat{I}$, the number of windings related to height n, the melt radius r_{me}, the Bessel function of n-th order $\mathcal{J}_n$ and:

$$p = \sqrt{-j\omega\mu\sigma} = (-1+j)^2 \cdot \frac{1}{\delta} \tag{11}$$

with the skin depth δ. Consequentially the averaged induced power density p_{ind} is a function of the temperature dependent electrical conductivity, is calculated by:

$$p_{ind}(\sigma(T)) = \frac{2}{r_{me}} \cdot \left| \int_{r_{me}} \frac{\vec{J}(r,\sigma) \cdot \vec{J}^*(r,\sigma)}{2\sigma} r \, \mathrm{d}\, r \right|. \tag{12}$$

Figure 4 depicts the characteristic of the induced power density as a function of the ratio of the melt radius r_{me} and the skin depth δ.

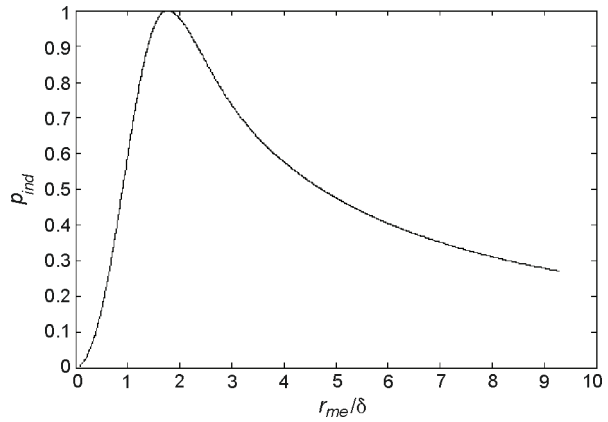

Fig. 4. Induced power inside the target material dependent on r_{me}/δ

For a successful heating process a preferable range of the ratio r_{me}/δ is $1 \le r_{me}/\delta \le 4$. To induce the maximum power inside the target material, the crucible radius r_{cr} can be adjusted with respect to the electrical conductivity and therefore to the skin depth of each target material. But an increase of the crucible radius will result in an increase of the coil inductance L. Regarding to the non-ferromagnetic characteristic of the target material and the crucible, the inductance is calculated as a short air-core coil by [11]:

$$L = \frac{\mu_0 \, \mu_r \cdot N^2 \cdot \pi \cdot r_{coil}^2}{h_{coil}} \cdot \frac{1}{1 + \frac{r_{coil}}{h_{coil}}}, \tag{13}$$

with the winding number N, the coil radius r_{coil} and the coil height h_{coil}. Under consideration of a resonance generator of constant power with a constant capacitor C, the output frequency f will decrease by the Thomson formula:

$$f = \frac{1}{2\pi \cdot \sqrt{LC}}. \tag{14}$$

As the coil current is directly proportional to the frequency it will also decrease. The induced power inside the target material UO_2 for different crucible radii is depicted in Figure 5 over a temperature range 300 K ≤ T ≤ 3210 K for $I(r_{me} = 50\text{ mm}) = 119$ A, $f(r_{me} = 50\text{ mm}) =$ = 2 MHz and $h_{me} = 100$ mm.

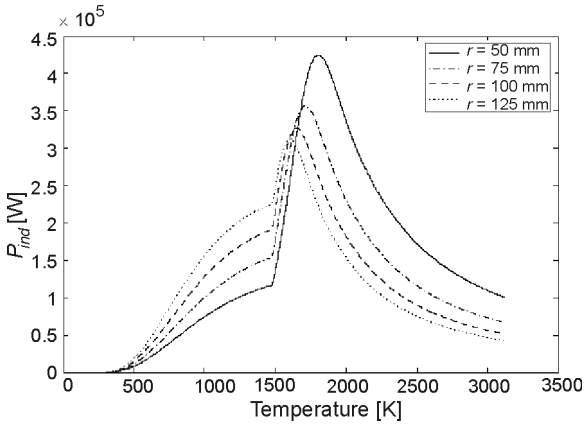

Fig. 5. Induced power inside the target material dependent on r_{me}

It can be seen that the induced power increases with the crucible radius for the first part of the temperature range. For higher temperatures, smaller radii are advantageous. The possibility to increase the induced power by decreasing the number of coil windings has only a weak influence of $1/\sqrt{N}$ with respect to the induced power inside the target material following from equations 10, 12 and 13.

4. Thermal field calculation

The temperature distribution inside the crucible has to be determined under consideration of transient thermal effects. The thermal field problem is described as:

$$\rho \cdot C_p(T)\frac{\partial T}{\partial t} = \nabla \cdot (\lambda(T) \cdot \nabla T) + \dot{q}(T), \tag{15}$$

with the induced heat $\dot{q}(T) = p_{ind}(T)$.

Due to the axis symmetric configuration the tangential temperature gradient is omitted, $\partial T/\partial \varphi = 0$.

By the nonlinear temperature dependent characteristic of the material properties and the induced heat, the thermal field distribution cannot be calculated analytically. Therefore an electromagnetic-thermal field coupling has to be performed, as it will be described in Section 5.

Despite the unknown temperature distribution, an analytical worst-case approximation of the thermal losses is performed. Thermal losses are expected due to heat flow through the sinter crust to the crucible as well as for heat radiation effects at the top of the melt.

Heat flow losses for the radial direction are estimated by [12]:

$$P_{loss,\,radial} = \frac{2\pi \cdot \lambda_{sc} \cdot h_{me} \cdot (T_{me} - T_{cr})}{\ln\left(\frac{r_{me} + w_{sc}}{r_{me}}\right)}, \tag{16}$$

with the thermal conductivity of the sinter crust λ_{sc}, the height of the melt h_{me}, the radius of the melt r_{me}, the width of the sinter crust w_{sc}, the temperature at the outer radius of the melt T_{me} and the crucible temperature T_{cr}. Heat losses due to the the bottom sinter crust in axial direction are estimated as:

$$P_{loss,\,axial} = (\pi \cdot r_{me}^2 \cdot \lambda_{sc}) \cdot \frac{(T_{me} - T_{cr})}{w_{sc}}. \tag{17}$$

The heat flow losses are directly proportional to the thermal conductivity of the sinter crust. As the temperature gradient of the thermal conductivity of UO_2 is negative in the lower temperature range an increase of the crucible temperature and following an increase of the sinter crust temperature has the positive effect of reduced heat flow losses, Figure 6a). The width of the sinter crust has another important impact on the heat flow losses. Heat flow losses will increase if the width of the sinter crust decrease. Heat radiation effects at the top of the melt are considered by Stefan Boltzmann's law:

$$P_{loss,\,radiation} = \varepsilon \cdot F \cdot \sigma_{SB} \cdot \pi \cdot r_{me}^2 \cdot (T_{me}^4 - T_{ir}^4), \tag{18}$$

with the emissivity ϵ the view factor F, which depends on the geometrical position and form of the irradiated areas, the Stefan Boltzmann constant $\sigma_{SB} = 5.67 \cdot 10^8$ W/m^{2}K^4 and the temperature of the irradiated area T_{ir}.

Thermal losses are depicted in Figure 6b) for the melt radius $r_{me} = 50$ mm, the melt height $h_{me} = 100$ mm, the width of the sinter crust $w_{sc} = 4$ mm, the constant thermal conductivity of the sinter crust $\lambda(T = 350\text{ K}) = 6.764$ W/mK, the temperature of the crucible T_{cr} and the irradiated areas T_{ir} of 350 K, the emissivity of a black radiator $\epsilon = 1$ with a viewing factor $F = 1$.

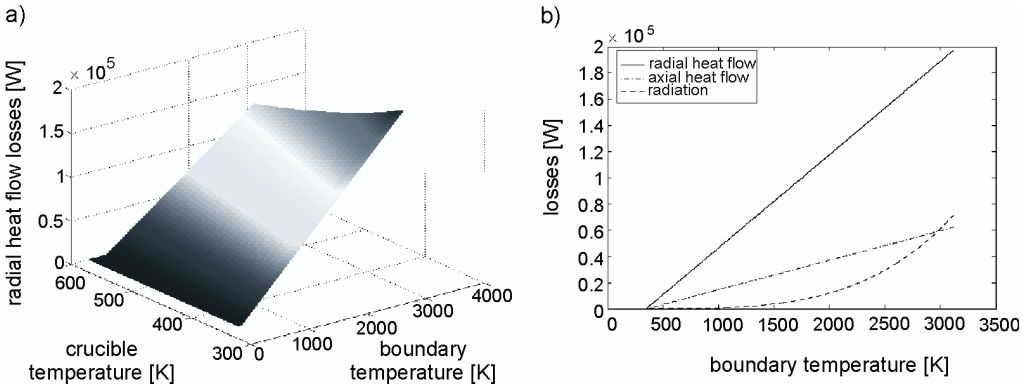

Fig. 6. Thermal losses: a) radial heat flow losses for different crucible temperatures, b) comparison of the thermal losses

Losses due to radial heat flow are dominant over the whole considered temperature range. At lower temperatures the axial heat flow losses are higher than the radiation losses. Not until a temperature of 2975 K the radiation losses bestride the axial heat flow losses. By increasing the crucible radius the thermal losses will also increase, as can be seen in equations 16, 17 and 18. Especially the axial losses increase quadratically with the melt radius.

5. Electromagnetic thermal fleld coupling

Under consideration of transient thermal effects and the nonlinear character of the temperature dependent material properties the electromagnetic and thermal field calculation is coupled.

The induced power density distribution is calculated by the harmonic one dimensional model (eq. 12). The temperature distribution is computed by an axis-symmetric finite element model. The outer boundaries of the sinter crust have a fixed temperature T_{cr}. The radiation losses are calculated by radiation elements considering Stefan-Boltzmann's law, equation 18, with a fixed temperature T_{ir}, as it is depicted in Figure 7.

It is assumed, that no power is induced into the sinter crust due to its direct cooling and its consequential minor electrical conductivity.

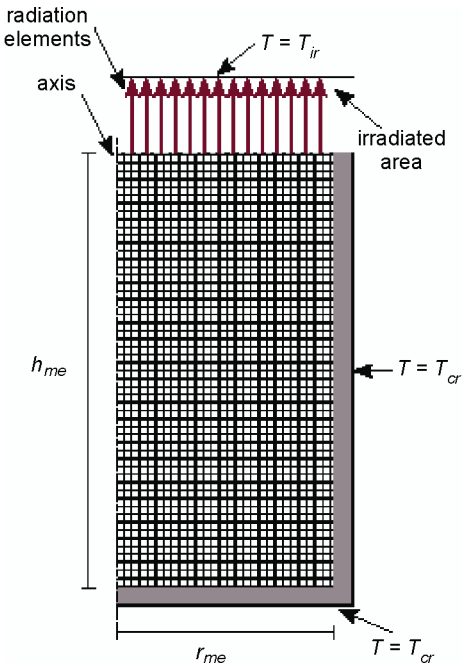

Fig. 7. Finite element model of the thermal computation

A flowchart of the coupled electromagnetic and thermal calculation is depicted in Figure 8. In a first step a look up table for the induced power depending on the temperature in a range of

350 K ≤ T ≤ 3120 K and the radial position of the finite elements of the thermal model is calculated.

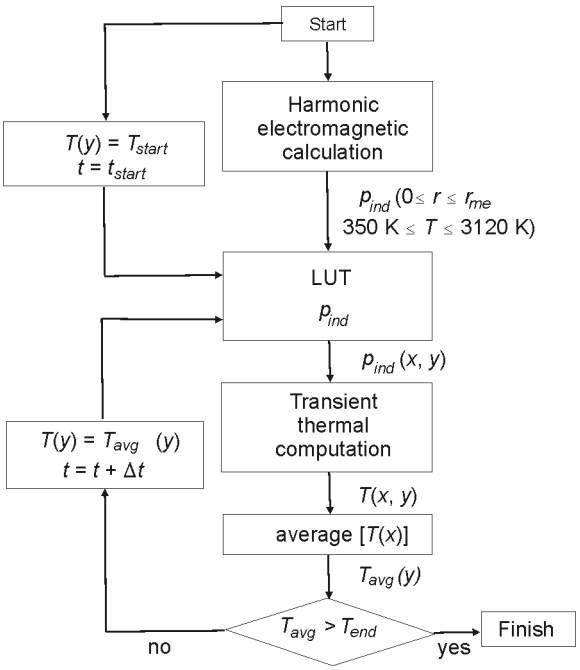

Fig. 8. Flowchart of the coupled electromagnetic and thermal field calculation

For the first time step the induced power for a given start temperature is applied to the thermal model. After each time step the temperature is averaged in radial direction for each axial position. Thus the temperature gradient in axial direction, resulting from axial heat flow and radiation losses can be considered.

The induced power is applied in dependency of the particular averaged temperature. The analysis stops if the averaged temperature T_{avg} exceeds a given end temperature T_{end}.

6. Results

A worst-case estimation of the applicability of the skull melting method for melting UO_2 is done by the before mentioned analytical models. The input data is given as: magnitude of coil current $\hat{I}(r_{coil=65\ \mathrm{mm}}) = 135.66\ \mathrm{A}$, current frequency $f = 1.61$ MHz, radius of the melt $r_{me} =$ $= 50$ mm, height of the melt $h_{me} = 100$ mm, width of the sinter crust $w_{sc} = 4$ mm, thermal conductivity of the sinter crust at crucible temperature T_{cr} (eq. 8), emissivity of a black radiator $\epsilon = 1$, viewing factor $F = 1$ and temperature of the irradiated area T_{ir}. Figure 9a) depicts the induced power inside the target material, the thermal losses and the resulting power for the heating process at outer temperatures $T_{cr} = T_{ir} = 350$ K. The thermal losses exceed the induced power at a temperature of $T = 367$ K for the first time. By this the heating process is

stopped. As it is depicted in Figure 6a) the dominant heat flow losses can be reduced by increasing the crucible temperature. Figure 9b) depicts the power for a less cooled crucible at a crucible temperature $T_{cr} = 400$ K. The thermal losses do not exceed the induced power until a temperature $T = 2254$ K.

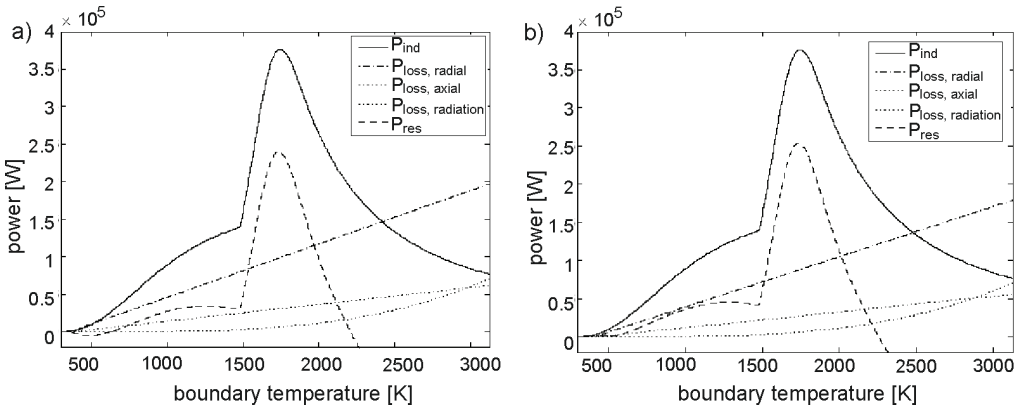

Fig. 9. Induced power, thermal losses and resulting power inside the target material: a) $T = 350$ K; b) $T = 400$ K

Based on this analytical estimation a coupled field analysis is performed. The crucible temperature and the temperature of the irradiated area is chosen as $T_{cr} = T_{ir} = 400$ K, the time step is $\Delta t = 1$ s. An energy balance is depicted in Figure 10. As predicted by the analytical model the main losses occur due to the radial heat flow through the sinter crust. Losses due to axial heat flow and radiation are marginal and can be neglected. The absorbed power by the target material is strongly increasing at time steps above 400 s due to the increased temperature and the increasing specific heat capacity.

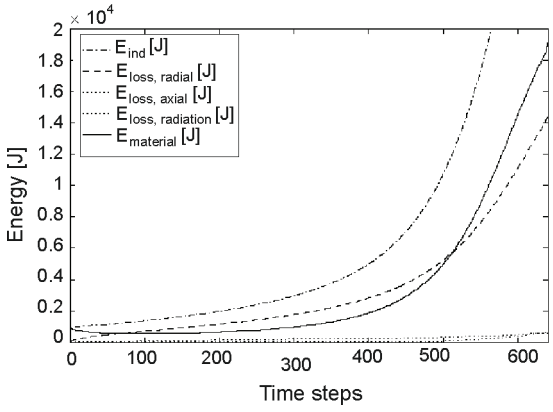

Fig. 10. Energy balance of the skull melting process

Figure 11 depicts the temperature distribution inside the target material at different time steps, without the sinter crust.

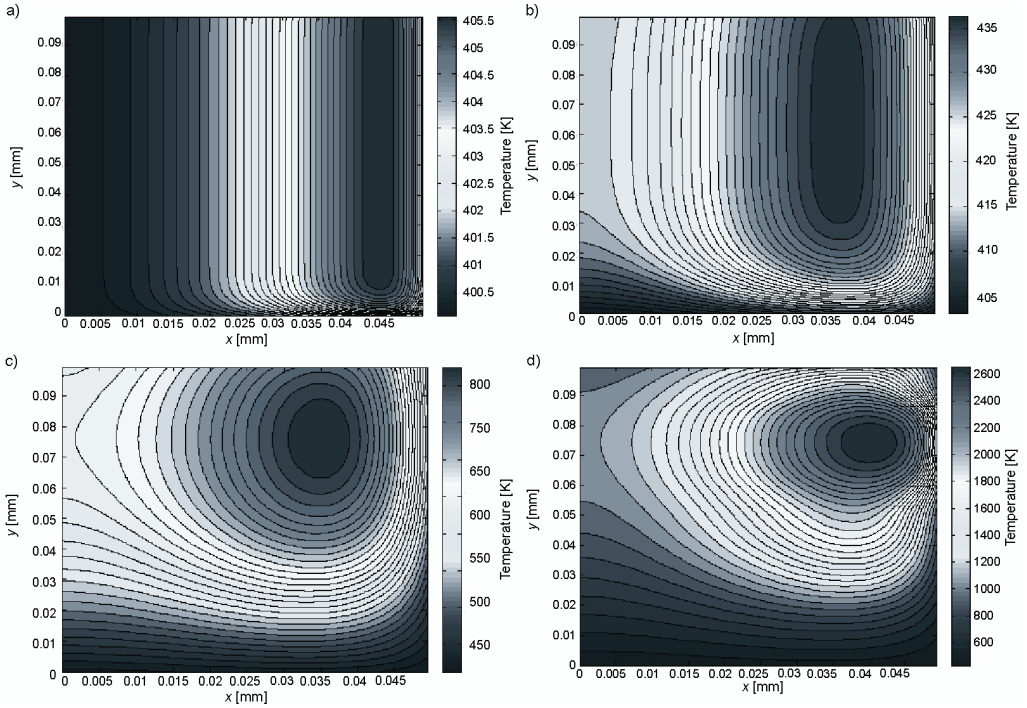

Fig. 11. Temperature distribution inside the target material at different time steps t:
a) t = 10 s; b) t = 100 s; c) t = 500 s; d) t = 600 s

Due to the heat flow through the sinter crust, the temperature at the inner boundary of the sinter crust is lower than it was assumed in the analytical loss estimation. Especially at high temperatures the analytical assumption is not valid. By the lower boundary temperature, the thermal losses will not exceed the induced power, as it is depicted in Figure 9b). An analysis with temperatures $T_{cr} = T_{ir} = 350$ K provides a non successful skull melting process despite the lower boundary temperature, for the given configuration.

7. Conclusion

This paper presents the electromagnetic and thermal calculation of the skull melting method for inorganic compounds, based on data of UO_2. Firstly the electromagnetic and thermal material properties of UO_2 are discussed. Based on this data the electromagnetic field distribution was analyzed analytically by a one dimensional harmonic model. The thermal losses of the skull melting process are analyzed by analytical equations. Radial heat flow losses through the sinter crust are dominant. An increase of the sinter crust temperature, due to a lower cooling of the crucible, reduces the losses because of the negative temperature gradient of the thermal conductivity of UO_2 at low temperatures ($T < 2000$ K).

Under consideration of transient thermal effects, a coupling of the electromagnetic and thermal field calculation is presented.

Closing results of a coupled field analysis are presented. A successful skull melting process is shown for outer temperatures $T_{cr} = T_{ir} = 400$ K.

References

[1] Wenckus J.F., Cohen M.L., Emslie A.G. et al., *Study, design and fabricate a cold crucible system.* Tech. Rep. Technical Report 75-0213, Air Force Cambridge Research Laboratories (1975).

[2] Assmus W., Whippey N., *Über das Skull-Schmelzen.* Chemie Ingenieur Technik 55(9): 716-717 (1983).

[3] Ronchi C., Sheindlin M., Musella M., Hyland G.J., *Thermal conductivity of uranium dioxide up to 2900 K from simultaneous measurement of the heat capacity and thermal diffusivity.* Journal of Applied Physics 85(2): 776 (1999).

[4] Fink J.K., *Thermophysical properties of uranium dioxide.* Journal of Nuclear Materials 279: 1-18 (2000).

[5] Bates J.L., Hinman C.A., Kawada T., *Electrical conductivity of uranium dioxide.* Journal of the American Ceramic Society 50: 652-656 (1967).

[6] Killeen J., *The effect of niobium oxide additions on the electrical conductivity of UO_2.* Journal of Nuclear Materials 88: 185-192 (1980).

[7] Casado J.M., Harding J.H., Hyland G., *Small-polaron hopping in mott-insulating UO_2.* Journal of Physics: Condensed Matter 6(25): 4685-4698 (1994).

[8] Blumenröder S., Brenten H., Zirngiebl E. et al., *Light scattering in heavy fermion compounds.* Journal of Magnetism and Magnetic Materials 76-77: 331-334 (1988).

[9] Hampton N., Saunders E., Saunders G. et al. *Frequency dependence of electrical conductivity and dielectric constant of UO_2.* Journal of Nuclear Materials 132: 156-159 (1985).

[10] Kotz J., Treichel P., Townsend J., *Chemistry and Chemical Reactivity*. Cengage Learning Services, (2008).

[11] Stöcker H., *Taschenbuch der Physik: Formeln, Tabellen, Übersichten*. Deutsch Harri Gmbh 5 (2004).

[12] Gross C., Assmus W., Muiznieks A. et al. *Power consumption of skull melting, part I: Analytical aspects and experiments.* Crystal Research and Technology 34(3): 319-328 (1999).